3D elastic multi-parameter FWI in foothills area: From numerical developments to applications

P T Trinh[1,2], M Appé[1], R Brossier[2], N Kamath[2], L Métivier[2,3] and J Virieux[2]

[1]Total EP, [2]Univ. Grenoble Alpes, ISTerre, [3]Univ. Grenoble Alpes, CNRS, LJK

Abstract

Full waveform inversion (FWI) of onshore targets is very challenging due to the complex free-surface-related effects and 3D geometry representation. In such areas, the seismic wavefield is dominated by highly energetic and dispersive surface waves, converted waves and back-scattering energy. We use a time-domain spectral-element-based approach for visco-elastic wavefield simulation in foothill areas. The challenges of the elastic multi-parameter FWI in complex land areas are highlighted through different case studies from the SEAM Phase II Foothill dataset. To mitigate the dominance of the V_s parameter over V_p , due to the presence of surface waves, we propose a two-steps data-windowing hierarchy to simultaneously invert for P- and S-wave speeds, focusing on early body waves before considering the whole data. By doing so, we aim at exploiting the maximum amount of information in the observed data and getting a reliable model parameters estimation, both in the near-surface and in deeper part. The prior information, introduced through the Bessel gradient smoothing and a non-linear model constraint on the relationship between compressional and shear velocities, plays an important role to mitigate the ill-posedness of the inversion process.

Introduction

Full waveform inversion (FWI) for onshore targets is very challenging due to complex free-surface-related effects and 3D geometry representation. In such areas, the seismic wavefield is dominated by highly energetic and dispersive surface waves, converted waves and back-scattering energy when the waves hit the steep slopes at the surface, or strong velocity contrasts. These complex effects cannot be fully removed or compensated by standard data pre-processing steps, implying that a correct description of the physics is strongly advisable for accurate model parameters estimation. Moreover, considering the complete physical phenomena of the wave propagation would make possible to take benefit of each piece of recorded data, for expected more accurate results and higher resolution. Adequate geometry representation is also required to honor the interaction between elastic waves and geological structures such as rapid topography variation and erosions. When considering complex structures or geological heterogeneities, regularization and preconditioning strategies also play an important role to mitigate the ill-posedness of the inversion problem (Guitton et al., 2012; Trinh et al., 2017).

In this paper, we present a fully integrated 3D visco-elastic FWI approach (SEM46 - Spectral Element Method for Seismic Imaging in eXploration code), dedicated to crustal-scale applications. The implementation is based on a time-domain spectral element method (SEM). Through different case studies, we highlight the importance of data-windowing hierarchy and prior information for a reliable reconstruction of V_p and V_s. We show that surface waves can be used as an additional source of information to enhance the model reconstruction.

Methodological Development in Sem46

SEM46 uses a classical hexahedra-based SEM frame (Komatitsch and Tromp, 1999) for wave modeling, where the physical domain Ω is decomposed into a set of non-overlapping hexahedral elements. The same mesh is used for the inversion steps. Each hexahedral element is further discretized into a set of $(N + 1)^3$ Gauss-Lobatto-Legendre (GLL) points, where N refers to the *interpolation order*. These collocation points are used to define $(N +1)^3$ basis functions; each function is a triple product of Lagrange polynomials of degree N.

Visco-elastic Wave Propagation

The viscoelastic wave propagation is performed under the consideration of constant quality factors $(Q_{IJ})_{I,J=1;\ldots;6}$ over the seismic frequency band, approximated by a set of L standard linear- solid (SLS) mechanisms at reference frequencies !. The contribution of each SLS in the approximation is described by the dimensionless anelastic coefficient y_v (Yang et al., 2016). Each SLS mechanism is associated with a memory variable field $\psi_{v;v=1;\ldots;L}$. Considering the choice of Lagrange basis functions and the GLL quadrature for numerical integration, the weak form of the partial differential equation (PDE) governing the visco-elastic waves propagation can be written as

$$\begin{cases} \mathbf{M}\partial_{tt}\mathbf{u} = - \mathbf{K}\mathbf{u} + D^{w} C^{a} \Sigma_{V=1}^{L} \Psi_{V} + \mathbf{F}, \\ \partial_t \Psi_V + \omega_V \Psi_V = \omega_V y_V D\mathbf{u}, \end{cases} \quad (1)$$

where the displacement field is denoted by **u**. The global mass and stiffness matrices are denoted respectively by **M** and **K**, and the source term by **F**. The global mass matrix **M** is diagonal by construction for SEM approaches. The operator D^w estimates the spatial derivatives of a vector in the Cartesian space. The operator D^w is equivalent to a spatial derivatives operator weighted by GLL weights. The quality factors Q_{IJ} are embedded inside the *attenuative stiffness matrix* $(C^a)_{6x6}$ as

$$C^{a}_{IJ} = C_{IJ} Q^{-1}_{IJ}; \quad (2)$$

where C_{IJ} are elastic stiffness coefficients.

The free-surface condition is naturally taken into account by the weak formulation. A second-order visco-elastic Newmark scheme is implemented for the time integration (Komatitsch, 1997; Trinh et al., 2019). The wavefield at the boundary is absorbed by a combination of sponge layers (Cerjan et al., 1985) and radiative boundary condition (Clayton and Engquist, 1977). The combination efficiently attenuates both short and long wavelength at a wide range of incident angles.

The inversion problem relies on the minimization of the least squares norm between the observed $\mathbf{d}_{obs}$ and the calculated data $\mathbf{d}_{cal}$ given by

$$\chi(\mathbf{m}) = \frac{1}{2} \| \mathbf{d}_{obs} - \mathbf{d}_{cal} \|^2 \quad (3)$$

In the time domain, the gradient of $\chi(\mathbf{m})$ with respect to the elastic tensor coefficients C_{IJ} can be computed through the adjoint-state approach (Plessix, 2006; Trinh et al., 2019)

$$\mathbf{g(x)} = \frac{\partial \chi(\mathbf{m})}{\partial C_{IJ}} = \left\langle \bar{\varepsilon}, \frac{\partial C}{\partial C_{IJ}} \varepsilon \right\rangle_{\Omega,t} - \left\langle \bar{\varepsilon}, \sum_{v=1}^{L} \frac{\partial C^R}{\partial C_{IJ}} \psi_v \right\rangle_{\Omega,t} \quad (4)$$

where $\bar{\varepsilon}$ and ε are respectively adjoint and incident strain fields. The gradient for any parameter (seismic velocity, anisotropic parameter ...) can then be computed by chain rule using the density ρ, C_{IJ} and Q^{-1}_{IJ} elementary gradients (Vigh et al., 2014)

$$\frac{\partial \chi}{\partial \alpha} = \frac{\partial \chi}{\partial \rho} \frac{\partial \rho}{\partial \alpha} + \sum_{I=1}^{6} \sum_{J=1}^{6} \frac{\partial \chi}{\partial C_{IJ}} \frac{\partial C_{IJ}}{\partial \alpha} + \sum_{I=1}^{6} \sum_{J=1}^{6} \frac{\partial \chi}{\partial Q^{-1}_{IJ}} \frac{\partial Q^{-1}_{IJ}}{\partial \alpha} \quad (5)$$

The gradient (5) is used as the input for any non-linear optimization process to solve the local minimization problem of the misfit function (3). Various non-linear optimization methods, coupled with the same line-search algorithm, are embedded through the SEISCOPE optimization toolbox (Métivier and Brossier, 2016).

Flexible Cartesian-based Mesh Design

To combine the accurate representation of topography, allowed by FE meshes, and the easiness of implementation of FD grid, our SEM46 package considers a Cartesian-based mesh design. The numbers of elements in *x, y* and *z* directions are constant, although the element size can vary. For the basis function at interpolation order $N = 4$ or 5, SEM allows to accurately model elastic waves propagation with around 5 GLL nodes per shortest wavelength (Komatitsch, 1997). This condition is referred as the *volume condition*.

When considering the presence of significant topography, hexahedral elements can be vertically deformed. For each element, a set of $(n + 1)$ control points in each direction is considered, leading to $(n+1)^3$ control points and associated shape functions in 3D. These shape functions are triple products of Lagrange polynomials of degree n. The number of control points and shape functions $(n + 1)$ is not related to the interpolation order N of the test functions needed for solving the wave equation. Representing the surface with P_1 shape functions (linear functions with $n = 1$) leads to the use of the eight corners of the element as control points. Such simple representation cannot honor sharp spatial variation of the free surface, as shown in one example in Figure 1A. The rough P_1

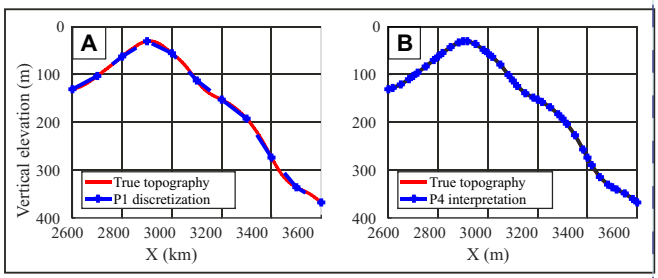

Fig. 1: Topography description of a 2D cross-section (extracted from SEAM II model) using (A) the eight corners of each element and P_1 shape function and (B) the $(4 + 1)^3$ GLL control points associated with P_4 shape functions. The element size is 100m in both case.

approximation of the topography affect the accuracy of the simulation due to the interaction between elastic waves and the complex surface. Figure 1B highlights that with the same size of the element (at 100 m), the P_4 shape function provides a better representation of the complex topography (i.e. $(4+1)^2$ GLL points are used in each element to capture the topography map, instead of $(1+1)^2$ points for the P_1 case). The mesh creation with P_n shape functions only affects the mesh construction, which is computed only once in the FWI workflow. The computational cost of the wavefield modeling is unaltered, while the simulation accuracy related to the complex wave-phenomena at the free-surface is significantly improved (Trinh et al., 2019).

In most geophysical targets, the velocity is spatially varying, leading to spatially varying wavelengths. The element size can thus be adapted to the variation of the expected local shortest wavelength. The reduction of the number of elements systematically reduce the numerical cost by the same factor, or even more if it induces the relaxation of the stability condition of the Newmark time-marching scheme.

Bessel Smoothing Filter

In practical applications, the gradient vector $\mathbf{g(x)}$ can exhibit unrealistic high-wave number components, which are incompatible with the intrinsic resolution of FWI. Designing a smoothing operator which can incorporate some prior knowledge of the geological structure, such as the local 3D rotation, becomes mandatory for practical applications (Guitton et al., 2012). To fulfill those requirements, we have introduced a structurally based nonstationary and anisotropic Bessel smoothing filter $B_{3D}(\mathbf{x})$, which can be directly and efficiently implemented on the SEM mesh. The anisotropic filter shape is defined by variable coherent lengths: $L_v(\mathbf{x})$ is associated with the direction perpendicular to the local bedding plan, $L_u(\mathbf{x})$ and $L_w(\mathbf{x})$ are related to the planar structure of potential geological features. The 3D orientation is controlled by azimuth $\theta(\mathbf{x})$ and dip $\varphi(\mathbf{x})$ angles (Trinh et al., 2017).

Instead of convolving the original vector $\mathbf{g(x)}$ with the forward filter $B_{3D}(\mathbf{x})$ to get the smoothed vector $\mathbf{s(x)}$, we solve the following equation relying on the sparse inverse operator

$$B^{-1}_{3D}(\mathbf{x}) * \mathbf{s(x)} = \mathbf{g(x)} \quad (6)$$

Due to the definition of the inverse operator, Equation (6) is equivalent to a Helmholtz-liked PDE. Under the assumption of slow spatial variation of the filter parameters, their spatial derivatives can be neglected. Equation (6) governing the smoothing process can be thus approximated as

$$\mathbf{s}(\mathbf{x}) - \nabla^{T}_{z;x;y}\ \mathbf{P}(\mathbf{x})\mathbf{P}^{T}(\mathbf{x})\nabla_{z;x;y}\mathbf{s}(\mathbf{x}) = \mathbf{g}(\mathbf{x}) \quad (7)$$

where the operator $\nabla_{z;x;y}$ is the spatial derivatives, and the upper symbol "^{T}" stands for the transposed operator. The information related to the geological variation of the medium (i.e. filter parameters) are embedded in the matrix

$$\mathbf{P}(\mathbf{x}) = \begin{bmatrix} L_v \cos\varphi & L_u \sin\varphi & 0 \\ -L_v \cos\theta \sin\varphi & L_u \cos\theta \cos\varphi & L_w \sin\theta \\ L_v \cos\theta \sin\varphi & -L_u \sin\theta \cos\varphi & L_w \cos\theta \end{bmatrix} \quad (8)$$

which can be interpreted as the projection between the Cartesian space and the locally rotated dimensionless coordinates system.

Following the weak formulation of SEM, Equation (7) naturally yields a symmetric, positive-definite and well-conditioned linear system

$$(\mathbf{M}_b + \mathbf{K}_b)\mathbf{s} = \mathbf{M}_b\mathbf{g} \quad (9)$$

The mass matrix $\mathbf{M}_b$ associated with the application of Bessel filter is diagonal, and the stiffness matrix $\mathbf{K}_b$ is symmetric by construction. We solve this linear system (9) through a matrix free parallel conjugate gradient iterative solver, using the same mesh and optimized kernels developed for the wave equation. The overall scheme has a linear algorithmic complexity with respect to the coherent length ($O(L)$), to be compared with the complexity $O(L^3)$ for standard windowed-convolution-based filter. In practical applications, the smoothing process can be performed at a negligible fraction of the computational cost of the forward/adjoint problems (less than 1%). A cascaded application can be used to produce other filter decays: for example, a double application of Bessel operators provides an accurate approximation of the Laplace filter (Trinh et al., 2017).

Model constraint on the ratio V_p/V_s

In many multi-parameter FWI applications, the gradient preconditioning operator might not be sufficient to stabilize the illposed inversion process. Therefore, multiple model constraints can be applied at each spatial position to remove any *unrealistic updates* in the inverted models. The constraints can be applied on each individual reconstructing parameter and/or on the relationship between parameters. Our current implementation considers simultaneously two constraints (Trinh et al., 2018)

- Bounds constraint C_1: V_p and V_s should vary within pre-defined ranges,
- Ratio constraint C_2: The ratio V_p/V_s should vary within a pre-defined range, for example $V_p/V_s \in [1.4 - 3.0]$.

The FWI problem can now be seen as the minimization of the misfit function (3) over a restricted model space, which is the intersection of two constraints

$$\mathbf{m} \in (C_1 \cap C_2). \quad (10)$$

These constraints can be designed based on well data or simple geological knowledge about the structure. The projection of model parameters onto the intersection of two constraints are performed through the Dykstra's algorithm, which ensures the uniqueness of the solution, independently with the order of the constraints application (Boyle and Dykstra, 1986; Peters and Herrmann, 2017; Trinh, 2018).

3D FWI APPLICATIONS

Elastic 3D configuration

We consider an isotropic elastic example coming from a 3D subtarget of the SEAM Phase II Foothill model (Regone et al., 2017). The maximal vertical variation of the topography is 800 m in this model. We use a 3D surface acquisition with 4 source-lines, each line including 20 sources, with inline and crossline source-spacing being ΔS_x = 320 m, ΔS_y = 500 m. For each source, a grid of 3-component (3C) receivers is deployed on the whole surface, the distance between two adjacent receivers being 12.5 m, providing a good 3D illumination. All sources are vertical point-force. The source-time function is a Ricker wavelet, centered at 3.5 Hz. The total recording time is equal to 6 sec. SEM is used for both forward and inversion problems. The observed data is generated with a constant element-size mesh, whereas the inversion problem is computed over a variable element-size mesh, locally satisfying the volume condition. The observed seismic wavefield is complex, including highly energetic and dispersive surface waves.

The initial V_p; V_s models are smoothed versions of the true model (Figures 2(b)). Similar smoothed model is used for the initial density. We invert simultaneously for V_p and V_s, and the density is kept unchanged. To mitigate the dominance of the V_s parameter over V_p, due to the presence of surface waves, we use a two-steps data-windowing hierarchy: (1) The early-body waves, arriving before the surfacewaves, are first considered for the inversion. (2) The reconstructed models will then be used as starting models for the inversion with the whole wavefield. We use a simple time-windowing to separate the early-body waves with the surface waves and the underlying reflected and backscattering waves. Each inversion step consists of 60 iterations of the *l*-BFGS optimization method. An anisotropic Bessel gradient filter is considered with parameters design as: vertical increases from L_V = 25 m; for the direction, L_u and L_w increase from 25m near the the unconformity position to 100 m elsewhere. The local 3D rotation is extracted from the true models. The constraint on ratio V_p/V_s is not necessary in this example.

The results are shown in Figure 2(c), where the inversion successfully recovers the main structures in both V_p and V_s models. Considering surface waves and other parts of the wave field does not degrade the V_p estimation and provide a high-resolution V_s model at both near-surface and deeper parts.

SEAM II Foothill Dip-line dataset

This example focuses on the SEAM Phase II pseudo-2D dipline visco-elastic survey, created by the SEAM consortium to reproduce the imaging challenges in mountain regions (Regone et al., 2017). We do not have any information about

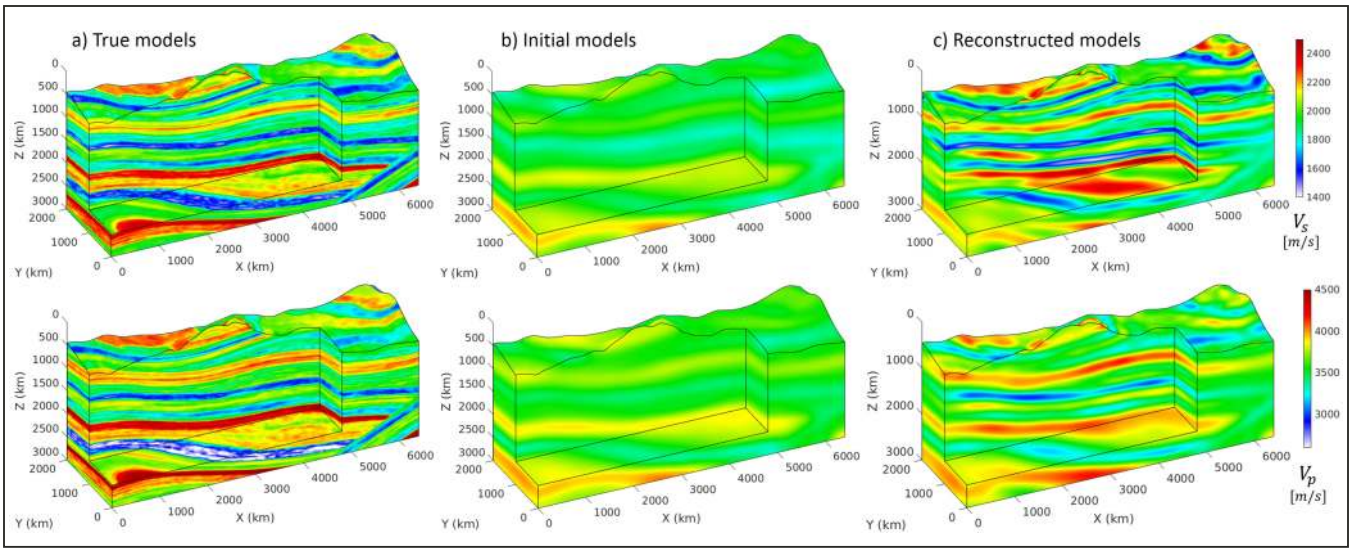

Fig. 2: Elastic 3D configuration: Top line - V_p models, bottom line - V_s models. (a) True models, (b) Initial models, (c) Reconstructed models.

the mesh generation or the input wavelet. The pseudo-2D line is acquired along the middle of the SEAM II Foothill model in the dip (x) direction. We limit the investigated area at 8 km in the x-direction as presented in Figure 3(a). The topography variation in this area has a maximal variation of 900 m. The near-surface has alluvial deposits, resulting from rapid erosion (Regone et al., 2017). These channels have low shear wave speed, about 550 m/s at the surface. The first 500 m below the surface has anelastic properties with $Q_p = Q_s = 50$.

The acquisition consists of one source line and 9 parallel receiver lines: the central line lies along the source line, with 4 parallel lines on either side, with inline and crossline receiver spacing being $\Delta R_x = 6{:}25$ m, $\Delta S_y = 25$ m (Oristaglio, 2016). All receivers are 3C geophones and the sources are vertical point-force. Due to limited computational resources, we only treat 40 shots, with source-spacing being 200 m. The acquired visco-elastic data is contaminated by highly energetic and dispersive surface waves due to the rapidly varying topography and the near-surface complexity. Significant back-scattering and converted energies are generated at the strong-contrast interfaces between the alluvial deposits and the background medium, which are the most challenging parts for data fitting (Trinh et al., 2018).

The initial V_p and V_s models are built from a standard interpolation between upscaling logs data at positions 0, 2, 4, 6 and 8 km in x -direction, as shown in Figure 3(b). To account for the 3D propagation effect, we consider a narrow 3D model with 2 km in y-direction. The 3D initial models are invariant along the y-direction. The density model is calculated from V_p through a linear regression obtained from wells data.

We invert simultaneously for V_p and V_s. The inversion is limited at 5 Hz, with two frequency bands [0-3 Hz] and [0-5 Hz]. The comparison between visco-elastic and elastic modelings shows insignificant difference, which implies that the elastic engine can be used to invert for this visco-elastic dataset. For each frequency band, a similar two-step data-windowing hierarchy as the previous example is considered: we firstly inject the early-body waves package then the entire wavefield. Each sequence contains 30 iterations, where the density and the source wavelet are kept unchanged. After each inversion sequence, the source wavelet and the density are re-estimated. The gradient preconditioning is performed through an anisotropic Bessel filter design, which is adapted to the working frequency:
$L_v = 100$m and $L_u = L_w = 400$m for [0-3 Hz]; $L_v = 30$m and $L_u = L_w = 120$m for [0-5 Hz]. We suppose that the smooth dip field is known and 0 strike as our main target is a 2D cross-section. In this example, the constraint on the relationship between V_p and V_s is mandatory to avoid unrealistic updates as $V_p/V_s \in$ [1.4 - 3.0].

The inverted V_s result is shown in Figure 3(c), where the alluvial deposits and structures both at the near-surface and

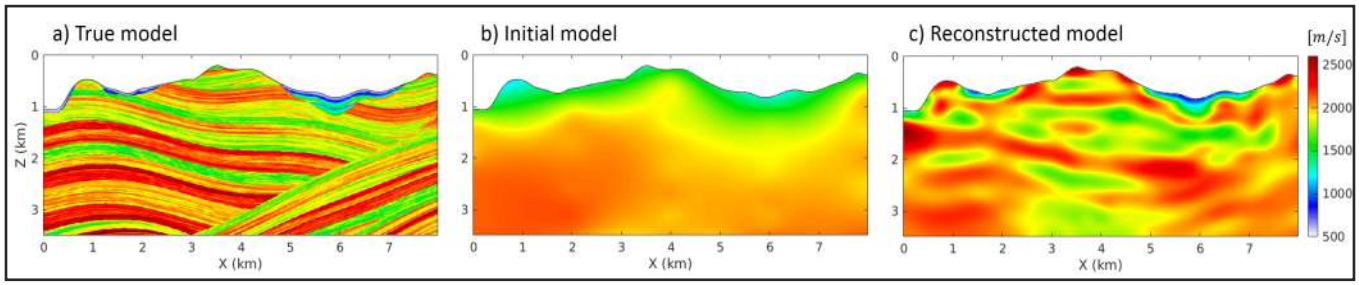

Fig. 3: V_s models in the SEAM II Foothill dataset case study: (a) True model, (b) Initial model, (c) Reconstructed model.

deeper part are well reconstructed. The inversion significantly improves the kinematic and waveform fitting between the calculated and the observed wavefield, that we do not show here (Trinh, 2018).

Conclusions and Perspectives

We present an integrated workflow capable of efficiently performing 3D elastic and visco-elastic time-domain FWI for multi-parameters, based on a SEM implementation. The prior information can be considered through the structure-oriented Bessel gradient preconditioning and multiple non-linear model constraints on reconstructed parameters and/or relationship between parameters. The challenges of the elastic multiparameter FWI in complex land areas are highlighted through different case studies, coming from the SEAM phase II Foothills benchmark. To mitigate the unequal sensitivity of the inversion process with respect to different parameters, we propose a two-step data-windowing strategy for a reliable simultaneous V_p and V_s estimation. If we can model the surface-related energies within half of the apparent wavelength, they can be used to improve the parameter estimation both at the near surface and deeper parts. Perspectives include alternative misfits design and large scale field data application.

Acknowledgments

The authors would like to thank Total E&P for financial support of PTT's PhD project, and for allowing to present and access the SEAM II Foothill model. This study, partially funded by the SEISCOPE consortium (http://seiscope2.osug.fr), was granted access to the HPC resources of the CIMENT center (https://ciment.ujf-grenoble.fr), CINES/IDRIS/TGCC (allocation 046091 of GENCI) and Pangea (TOTAL S&A). Authors enjoy discussions with L. Lemaistre, B. Duquet, J.L. Boelle and P. Williamson.

References

Boyle, J. P., and R. L. Dykstra, 1986, A method for finding projections onto the intersection of convex sets in Hilbert spaces, *in* Advances in Order Restricted Statistical Inference: Proceedings of the Symposium on Order Restricted Statistical Inference held in Iowa City, Iowa, September 11–13, 1985: Springer New York, 28–47.

Cerjan, C. D., D. Kosloff, and M. Reshef, 1985, A non-reflecting boundary condition for direct acoustic and elastic wave equations: Geophysics, **50**, 705–708.

Clayton, R., and B. Engquist, 1977, Absorbing boundary conditions for acoustic and elastic wave equations: Bulletin of the Seismological Society of America, **67**, 1529–1540.

Guitton, A., G. Ayeni, and E. Díaz, 2012, Constrained full-waveform inversion by model reparameterization: Geophysics, **77**, R117–R127.

Komatitsch, D., 1997, Méthodes spectrales et éléments spectraux pour l'équation de l'élastodynamique 2D et 3D en milieu hétérogène: PhD thesis, Institut de Géophysique du Globe de Paris.

Komatitsch, D., and J. Tromp, 1999, Introduction to the spectral element method for three-dimensional seismic wave propagation: Geophysical Journal International, **139**, 806–822.

Métivier, L., and R. Brossier, 2016, The SEISCOPE optimization toolbox: A large-scale nonlinear optimization library based on reverse communication: Geophysics, **81**, F11–F25.

Oristaglio, M., 2016, Land Seismic Challenges wraps up with Foothills model: The Leading Edge, **35**, 292–293.

Peters, B., and F.J. Herrmann, 2017, Constraints versus penalties for edge-preserving full-waveform inversion: The Leading Edge, **36**, 94–100.

Plessix, R. E., 2006, A review of the adjoint-state method for computing the gradient of a functional with geophysical applications: Geophysical Journal International, **167**, 495–503.

Regone, C., J. Stefani, P. Wang, C. Gerea, G. Gonzalez, and M. Oristaglio, 2017, Geologic model building in SEAM Phase II - Land seismic challenges: The Leading Edge, **36**, 738–749.

Trinh, P.T., 2018, 3D Multi-parameters Full Waveform Inversion for challenging land targets: PhD thesis, University Grenoble Alpes.

Trinh, P. T., R. Brossier, L. Métivier, L. Tavard, and J. Virieux, 2019, Efficient 3D time-domain elastic and viscoelastic Full Waveform Inversion using a spectral-element method on flexible Cartesianbased mesh: Geophysics, **84**, R75–R97.

Trinh, P. T., R. Brossier, L. Métivier, and J. Virieux, 2018, Data oriented strategy and Vp/Vs model-constraint for simultaneous Vp and Vs reconstruction in 3D viscoelastic FWI: Application to the SEAM II foothills dataset: Presented at the 88th SEG Conference and Exhibition 2018, Anaheim.

Trinh, P. T., R. Brossier, L. Métivier, J. Virieux, and P. Wellington, 2017, Bessel smoothing filter for spectral element mesh: Geophysical Journal International, **209**, 1489–1512.

Vigh, D., K. Jiao, D. Watts, and D. Sun, 2014, Elastic full-waveform inversion application using multicomponent measurements of seismic data collection: Geophysics, **79**, R63–R77.

Yang, P., R. Brossier, L. Métivier, and J. Virieux, 2016, A review on the systematic formulation of 3D multiparameter full waveform inversion in viscoelastic medium: Geophysical Journal International, **207**, 129–149.